Development and quality characterization of a novel CT system

Alexander A. Schegerer[a], Martin Lingenheil[a], Matthias Klaften[b], Thomas Förster[a], Martin Hrabé de Angelis[b], and Christoph Hoeschen[a]

[a] Helmholtz Zentrum München, Institute for Radiation Protection, Ingolstädter Landstraße 1, 85764 Neuherberg, Germany;

[b] Helmholtz Zentrum München, Institute for Experimental Genetics, Ingolstädter Landstraße 1, 85764 Neuherberg, Germany

ABSTRACT

Novel geometrical designs of computed tomography (CT) scanners in combination with novel image reconstruction algorithms promise to reduce ionizing radiation exposure to the patient in CT scans. While the sampling density of the Field Of View (FOV) is retained, the image quality can even be increased in contrast to conventional CT scanners. In this study, we present first images obtained with a novel CT scanner that we developed in our working group. In this open CT system with irradiation within a fan beam, parallel Radon data are directly obtained for image reconstruction using the OPED (Orthogonal Polynomial Expansion on the Disk) algorithm. This algorithm uses Radon data directly, i.e., without any further data processing such as rebinning and interpolation. We experimentally test theoretical predictions for this system by quantifying image quality parameters in comparison with corresponding parameters that are derived from the images of a conventional scanner of the 3rd generation. The modulation transfer function (MTF) and noise power spectrum (NPS) are determined using a test phantom. The novel CT system quantitatively shows the same noise property as the conventional scanner. The resolution that is reached in the center of a reconstructed image is nearly identical for both scanner types. But we found that the resolution that is achieved in the novel CT system does not depend on the image position while the MTF of the conventional scanner decreases for radially outer regions of the image.

Keywords: computed tomography (CT), CT design, micro CT, image reconstruction algorithm, FBP, OPED, image quality, MTF, NPS

1. INTRODUCTION

CT has strongly accelerated and improved medical diagnosis. Although the resolving power of CT scanners has impressively increased for all dimensions in the recent decade, the number of concerns of scientists about the disproportionate increase of radiaton exposure due to CT diagnostics has increased. In fact, the radiation exposure that is obtained in radiological applications has increased by more than 20% in Germany during the recent decade, and this development can solely be ascribed to CT diagnostics as the effective dose resulting from other radiological applications has even decreased.[1–5] In Germany, more than 90% of the man-made collective effective dose of $\sim$2.0 mSv/year can be ascribed to medical applications from which 56% results from CT diagnostics. However, only 7% of all German radiological applications arise from CT investigations. In other industrialized countries the radiation exposure from CT scans has similarly increased.[5,6]

Therefore, an exact coverage of the medically interesting target volume by the radiation field, reasonably low exposures, and the application of alternative diagnostic methods beyond CT diagnostics should be considered.[6] Moreover, there are novel scanner designs and image reconstruction algorithms that promise to reduce the ionizing radiation exposure of patients in clinical practice without reducing the diagnostic value of CT images.

Send correspondence to A. A. Schegerer E-mail: alexander.schegerer@helmholtz-muenchen.de, fax: +49 89 3187 19 3886

Medical Imaging 2010: Physics of Medical Imaging, edited by Ehsan Samei, Norbert J. Pelc,
Proc. of SPIE Vol. 7622, 762230 · © 2010 SPIE · CCC code: 1605-7422/10/$18 · doi: 10.1117/12.844175

Downloaded From: http://proceedings.spiedigitallibrary.org/ on 08/02/2016 Terms of Use: http://spiedigitallibrary.org/ss/TermsOfUse.aspx

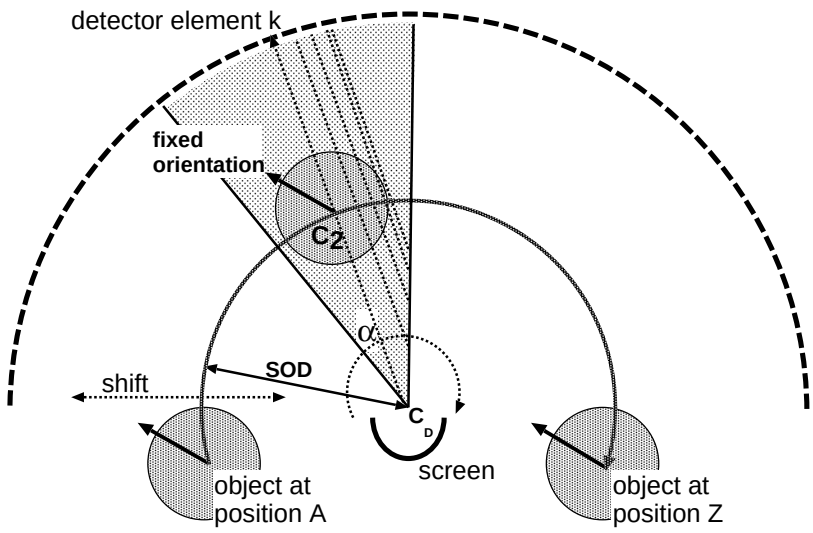

Figure 1. In the watch geometry, the object starts at position **A** and moves on a circular trajectory around the source. The dotted lines represent some sampling steps of a single projection whose line integrals are acquired by subsequent readouts of the same detector element k ($k \in [0; N_{\mathrm{det}}]$). It is characteristic for the OPED algorithm that the distances of subsequent sampling steps decrease close to the limitations of the radiation field.

The potential advantages of the OPED image reconstruction algorithm in acquiring and reconstructing tomographic data sets were presented in previous SPIE Medical Imaging conferences.[7,8] OPED is a numerically stable algorithm. Images that were reconstructed with OPED are characterized by a small global error and high resolution. Furthermore, the image reconstruction made with OPED can be implemented with a number of operations of the same order as the conventionally used Filtered Back Projection (FBP) algorithm. The number of operations in the OPED algorithm can even decrease.

Two novel CT scanners, i.e., the CT with Dual Optimal Reading (CT D'OR) and another CT scanner design that is based on the "watch geometry" have recently been developed and constructed.[9–11] These novel CT designs are adapted to the OPED algorithm.[12] In comparison with conventional methods, previous theoretical studies have predicted a dose reduction for these novel CT systems. The image quality can simultaneously be retained or even increased by contrast enhancement for a constant sampling density of the FOV.[11,13]

The potential advantages that were theoretically predicted for the novel CT design that is based on the "watch geometry" are experimentally quantified in this study. In Sect. 2.1, we present the basic design of the novel scanner while the assembly of our lab model is precisely described in Sect. 2.2. The methods used for the characterization of the scanner and our experimental set-up are shown in Sect. 3. The results of our measurements of quality parameters are presented and discussed in Sect. 4 before a final conclusion is derived in Sect. 5.

2. NOVEL CT DESIGN

2.1 The watch geometry and trajectory

The inner surface of a half ring detector system of the CT design that is presented in this study is continuously covered with detector elements (Fig. 1). The X-ray source is fixed in the center C_{D} of the detector ring while the orientation of the radiation field with a fan angle α accompanies the object on its circular way around the source. The focal spot of the source rotates in C_{D}. The spatial orientation of the investigated object is fixed. The object starts at position **A** and ends at position **Z**, i.e., the object covers an arc length of $(\pi + \alpha) \times SOD$ during a scan. Corresponding to conventional methods, an arc angle of $(\pi + \alpha)$ is sufficient for image reconstruction using the OPED algorithm. The Source-Object-Distance SOD of the trajectory can easily be modified in subsequent scans resulting in an increase/decrease of the projection size of an object on the detector and, therefore, in a modification of the spatial resolution before image reconstruction. The exposure dose of the object

Downloaded From: http://proceedings.spiedigitallibrary.org/ on 08/02/2016 Terms of Use: http://spiedigitallibrary.org/ss/TermsOfUse.aspx

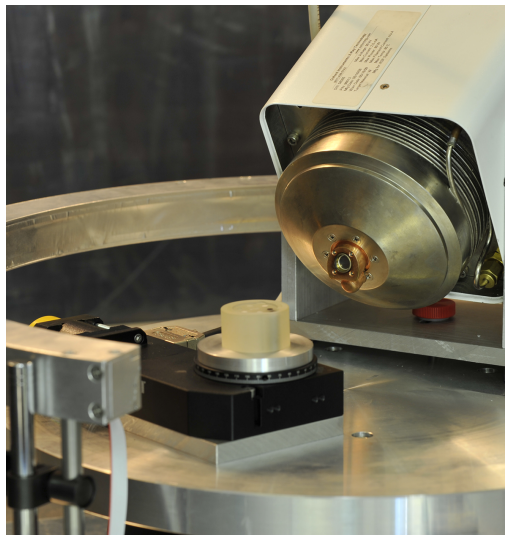

Figure 2. The basic components of the lab model of the novel CT scanner, i.e., the half-ring detector and the central X-ray tube are shown in the photography. The distance between object, source, and detector can be modified to change resolving power. An acryl glass cylinder on a rotary table is scanned in the photography.

is simultaneously changed considering the quadratic decrease of the exposure dose with increasing distance from the source.

A half ring screen in the center can prevent the irradiation of the object in the lower semicircle region where no detector element exists. Any detector element k of the upper semicircle region ($k \in [0; N_{\mathrm{det}}]$), where N_{det} is the number of detector elements on the detector ring, acquires all the parallel data for a specific projection angle. The distances of subsequent sampling steps of a projection decrease close to the limitations of the radiation field.[7,8] Such a tomographic sampling mode is the outcome of a scan with the novel CT scanner as well as of a conventional scanner after data reordering. This tomographic sampling mode is required by the OPED algorithm. But the image that is obtained from a scan in the watch geometry can also be reconstructed using the FBP algorithm.[14,15]

We finally have to mention that the identical tomographic data set can also be acquired by the alternative scan process where the object, e.g. a person/animal, is fixed while the source detector system moves on a circular orbit around the object.[11]

CT scanners available on the market contain either a form of the 3rd generation scanner system, a flat panel detector, or an X-ray camera for data collection. The novel CT geometry that is based on the watch geometry has advantages over existing CT systems. Using parallel projections instead of a fan beam geometry, the data samples exactly fit the line integrals required by the OPED algorithm. Therefore, data processing such as rebinning and interpolation that is generally necessary for image reconstructions using the conventional FBP algorithm is omitted in the novel geometry.[16]

2.2 The scanner assembly

The concept for the novel CT scanning geometry described in the previous section is realized in a demonstrator of a one-slice micro CT scanner in our laboratory. A photography of the assembly is shown in Fig. 2.

The detector consists of a steel housing that is shaped as a ring segment with an arc angle of 240° and an inner radius of $SDD = 23\,\mathrm{cm}$. The housing contains 13 photosensors (Texas Advanced Optoelectronic Solutions Inc., Plano, TX, USA) coated with YAG:Ce scintillation layers (Crytur Ltd., Turnov, Czech Republic). To prevent the detection of ambient light, we covered the front of the sensor modules with a thin ($\sim$20 μm) aluminum foil.

Each sensor module consists of 768 photodiodes with a pixel spacing of 63.5 μm. A pixel has a size of 63.5 μm $\times$ 55.5 μm. The pixels of a single module thus cover an angle of 12.1° on the ring detector. Due to the

Downloaded From: http://proceedings.spiedigitallibrary.org/ on 08/02/2016 Terms of Use: http://spiedigitallibrary.org/ss/TermsOfUse.aspx

design of the sensor modules, there is a gap of 3.5° between their sensitive areas. The 13 sensor modules cover the central 200° of the detector ring in a polygonal fashion where sensitive areas alternate with detector gaps. The gaps in the data set of a single scan can be filled by another data set that is obtained from a subsequent scan where the orientation of the object at the start position is slightly changed by more than the gap angle of 3.5°. Then, both data sets are interlaced using the correlation relation in Fourier space.[17] The latter method is tested by a corresponding routine in position space.

We choose a detector integration time of 100 μs. Subsequent readouts start after a dead time of another 100 μs. To eliminate characteristics of the detector modules in the data sample, each scan E is flatfielded using an air scan E_0 after exposures B of the dark current have been subtracted. The same scan parameters were used for E, E_0, and B. The attenuation coefficient μ can thus be derived from

$$\mu = \log_{10}\left(\frac{E_0 - B}{E - B}\right). \tag{1}$$

The scanner assembly further consists of two rotary tables. A micro focus X-ray tube (Oxford Instruments X-Ray Technology Inc., Scotts Valley, CA, USA) is fixed on a primary rotary table (MiCos GmbH, Eschbach, Germany). The X-ray spot is supposed to have a diameter of 17 μm. The center of the primary table, i.e., the focus of the X-ray tube coincides with the center C_{D} of the detector ring. The secondary table (MiCos GmbH, Eschbach, Germany) that carryies the object is mounted at C_2 at a radius of $SOD = 12.7$ cm in our experiments. In the watch geometry, the primary and secondary tables counterrotate with an angular velocity of $\omega = 0.25°/\mathrm{s}$. When operating as a 3rd generation CT-scanner, only the secondary table rotates with a velocity of ω (Sect. 3.2). The accuracy of the alignment of the source detector system is in a range of 0.1 mm.

In our experiments, the X-ray tube has a beam quality of 60 kVp. The anode material of the tube is tungsten. A maximum power of 60 W can be reached. The fan angle of the radiation field is ∼41°. After the passage through a 245 μm beryllium window, radiation additionally passes a 300 μm Al absorber to reduce the spectral width which would otherwise result in beam hardening artifacts in the reconstructed images.[18]

3. METHODS

3.1 Image quality parameters

The formation of an image I can mathematically be described by a sum of the noise function N, artifacts A, and the object function O that is convolved with the Point Spread Function PSF, i.e.,

$$I = O * PSF + N + A. \tag{2}$$

The PSF is determined by the sampling density, the image reconstruction algorithm, and the FOV shown by the reconstructed image.[19] The term N is a sum of quantum noise and detector noise. Anatomical noise is not considered in our experiments. As anatomical noise can exceed the level of detector noise and quantum noise, the noise component that is derived in our experiments is assumed to be a lower limit.[20] Artifacts are not subject matter in this study.

The quantities PSF and N are analyzed in frequency space after their Fourier transformation to the Modulation Transfer Function (MTF) and the Noise Power Spectrum (NPS), respectively. We assume a linear, space-invariant system, but we have to mention that these requirements are only locally fulfilled.[21–23]

There are several approaches to determine the resolution that is modified in the image formation chain. The spatial resolution of the reconstructed image is conventionally derived from an image of a small diameter metal wire.[24] However, as the MTF of the image is also limited by the sampling pitch, including detector pitch and pitch of the displayed matrix, we propose to determine the *presampled* MTF by using an edge device from that the Edge Spread Function (ESF) can be derived.[25] A slightly tilted edge in the digitized CT image allows a finer sampling and, therefore, the determination of the *presampled* MTF.[26,27] Using such a method, the effective sampling distance becomes smaller than the original pitch of the digitized image and the effect of digitization is reduced. The ESF is differentiated to obtain the Line Spread Function (LSF). This approach has to be mathematically corrected for the frequency passband of the finite-element differentiation of the sampled data.[28]

Downloaded From: http://proceedings.spiedigitallibrary.org/ on 08/02/2016 Terms of Use: http://spiedigitallibrary.org/ss/TermsOfUse.aspx

The proposed method using an edge device for the determination of the MTF corresponds to the methods of quality characterization in projection radiography.[29]

A potentially homogeneous region of the reconstructed $N_x \times N_y$-sized CT image $I(x, y)$ is used for the determination of the NPS. In order to correct for potential, global nonuniformities caused by the Heel effect, we fit a second-order polynomial $S(x, y)$ to $I(x, y)$. This polynomical $S(x, y)$ is subtracted from $I(x, y)$.[30] After a subdivision of the resulting Region Of Interest (ROI) in 32×32 pixel-sized regions, the two-dimensional NPS can be computed using the autocorrelation function

$$NPS(u, v) = \frac{p_{\mathrm{x}} p_{\mathrm{z}}}{32 \times 32} \left| \sum_{i=1}^{32} \sum_{k=1}^{32} [I(x_i, y_k) - S(x_i, y_k)] \exp[-2\pi j(u_i x_i + v_k y_k)] \right|^2, \tag{3}$$

where j is the imaginary unit.[31] The parameters p_{x} and p_{z} stand for the pixel pitches of the image $I(x_{\mathrm{i}}, y_{\mathrm{i}})$. The parameters u and v are coordinates in Fourier space. The one-dimensional NPS can finally be obtained from the two-dimensional NPS. For this, 14 adjacent rows/columns of the axes of the two-dimensional NPS are interlaced to an one-dimensional vector. For each (u,v) coordinate pair of these rows/columns, the corresponding spatial frequency is determined using $\sqrt{u^2 + v^2}$. Corresponding to previous approaches, the axes of the two-dimensional NPS are omitted.[30]

3.2 Experimental set-up

Parallel data sets can directly be obtained by the watch trajectory. But in a subsequent scan, the CT design and the object trajectory can be modified to produce the conventional fan data set that is identical to a conventional 3rd generation scanner. The images are reconstructed using the OPED and the FBP algorithm, respectively. For the FBP algorithm, the default saw tooth reconstruction filter is applied. We use a commerically available FBP routine for the image reconstructions from the conventional fan data sets.

Due to a maximum rotation angle of the rotary table of the object of $\ll 360°$, only a $\sim 240°$ scan of the 3rd generation geometry can finally be obtained in our experiments. The missing data for a full 360°-set is completed by the corresponding data that are obtained at projection angles of $<180°$. Such an approach is possible after the fan data set were resorted to the corresponding parallel data set by the FBP algorithm. Parallel data at a projection angle θ and ray t corresponds to data at a projection angle of $\theta + 180°$ and ray $-t$. For the latter relation it is necessary that the center line, i.e., the line that always crosses the same point of the FOV during the scan, crosses the center of the detector unit of the 3rd generation geometry.

As the sampling density of the FOV should be identical, the number of views and rays (detector elements) of the 3rd generation scan should be adapted to the number of read-outs (projections) and detector elements of the scan of the watch trajectory. Furthermore, the total dose emitted during the scans should be identical. To reduce noise in the resulting images that is caused by the low power of the X-ray source, rows and columns in both resulting data sets are rebinned. Scan parameters and the size of the resulting data sets that are used for image reconstruction are listed in Table 1.

We use a potentially homogeneous ROI within the 1 cm $\times$ 1 cm-sized cross section of an acrylic glass cube for the determination of the NPS in both geometries. An image of this cube that is slightly tilted by $\sim 4°$ is used for the determination of the ESFs. In subsequent scans, the cube is located at different positions within the FOV to determine the dependency of MTF and NPS on the position in the reconstructed image. Figure 3 shows the resulting images from the watch scans and the 3rd generation scans. Circular artifacts result from an incomplete elimination of different sensor characteristics of the 13 photodiodes by the corresponding flatfields E_0 (Sect. 2.2). Radial artifacts at the edges of the cube arise from scattering.

4. RESULTS

Figure 4 shows the MTF derived from scans of the watch geometry and the conventional 3rd generation geometry. The images were reconstructed using the OPED algorithm and the FBP algorithm, respectively. The noisy MTFs at larger spatial frequencies ($> 15\,\mathrm{mm}^{-1}$) arise from the low power of the X-ray tube used. Therefore,

Downloaded From: http://proceedings.spiedigitallibrary.org/ on 08/02/2016 Terms of Use: http://spiedigitallibrary.org/ss/TermsOfUse.aspx

Table 1. Parameters of the 3rd generation scans and the scans that are based on the watch trajectory are listed in this table. The symbols N_{proj} and N_{det} describe the number of views in the 3rd generation scan and read-outs in the watch scan as well as the number of detector elements, respectively. They correspond to the number of rows and columns in the data sets. The number of detector elements within the fan beam α for the 3rd generation scans and on the whole detector ring (within 200°, Sect. 2.2) for the scan in the watch geometry are listed. The abbrevation SDD is an acronym for Source Detector Distance.

	3rd generation	watch geometry
SDD	23.0 cm	
SOD	12.7 cm	
α	41°	
p_x	0.0055 cm	
p_z	0.0063 cm	
N_{proj}	1257	261
N_{det}	261	1257

we determine an averaged ESF from the ESFs derived from a single edge of the cube before its Fourier transformation to the MTF.[32]

In the center position of the cube in the image, the MTFs of the different geometries only slightly differ (panel MTF-2). But the MTFs derived from the off-center position of the cube strongly depends on the scan geometry (panel MTF-1). The local maxium at $\sim 15\,\mathrm{mm}^{-1}$ of the MTF from the conventional scan of the excentric cube position can probably be ascribed to noise.

We conclude that the MTFs that are derived from the images of the watch geometry (*light gray lines* in Fig. 4) does not depend on the position in the corresponding image. But the MTFs that are derived from the conventional scans radially decreases as it has already shown by a previous study.[33] This finding can be explained by the interpolation of the fan data set to the Cartesian grid of the image. Such an interpolation is omitted for the watch geometry as it is adapted to the OPED algorithm. Indeed, samples of fan data generate a nonuniform grid in parallel beam coordinates, and its nonuniformity is even higher when the fan angle becomes larger. The fan data of the conventional scan is commonly parallelized for reducing computation time and increasing numerical stability. A sinusoidal relation whose zero point is centered at the center line is used for the parallelization.[14,15] As a consequence, the sampling density of the FOV remains constant for smaller ray angles within the fan angle and does not correspond to the actual density of the data acquired. Information of the original data can be lost and the contrast at a discontinuous transition of a sharp edge at outer ROIs of the FOV can be reduced, therefore.

As mentioned in Sect. 2.1, the sampling density at off-centered projections *in*-creases in the watch geometry that theoretically results in an increase of the MTF.[7,8] However, such an effect cannot be noticed by the measurements (Fig. 4) probably because of noisy data and the low number of projections used (Table 1).

Figure 5 shows the NPS derived from scans of the watch geometry and the conventional 3rd generation geometry for different positions of the homogeneous acrylic cube in the image. The NPS only slightly depends on the image position where the NPS is derived. The NPS of the conventional scan that is determined in the image center is slightly larger than the other NPS for smaller spatial frequencies. Remnants of detector characteristics that could not completely be removed by the flatfield E_0 in the central region (Sect. 2.2, Fig. 3) could be responsible for this increase.

5. CONCLUSION

In this study, we presented physical image quality measurements of a novel CT system that is based on the watch geometry. In this scanner system, a parallel data set is directly obtained before the corresponding image is reconstructed using the OPED algorithm. The novel CT system is adapted to this algorithm although image

Downloaded From: http://proceedings.spiedigitallibrary.org/ on 08/02/2016 Terms of Use: http://spiedigitallibrary.org/ss/TermsOfUse.aspx

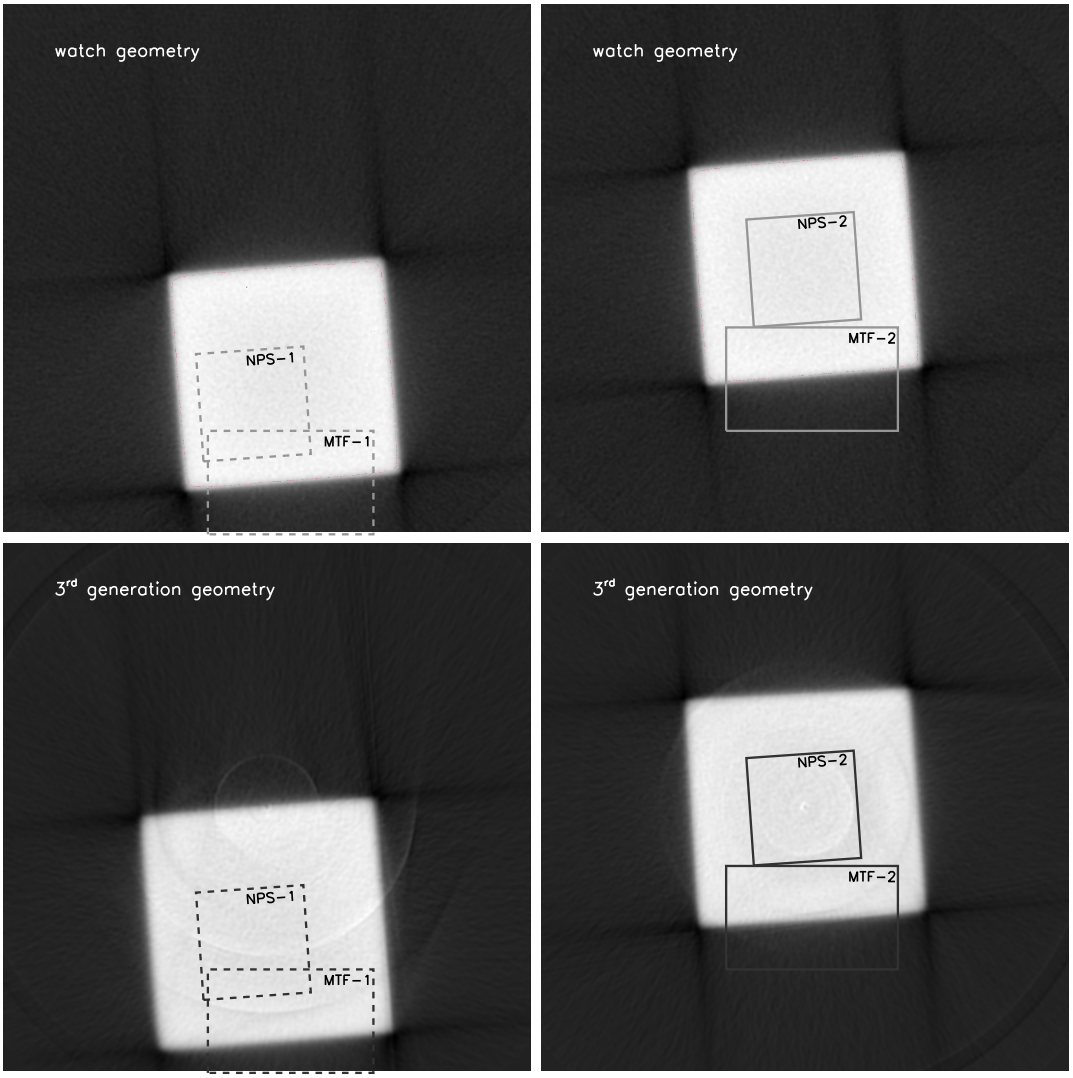

Figure 3. These images show the reconstructed images derived from scans that are based on the watch trajectory (*upper row*) and 3rd generation trajectory. The *right* images are reconstructed from scans where the acrylic cube is centered in the FOV. *Dark gray* and *light gray* framed boxes represent ROIs that are used for the determination of NPS and MTF derived at different positions in the image. See Sect. 3.2 and Sect. 4 for further explanations.

reconstructions are also possible using the FBP algorithm. We scrutinized the characteristics of the watch geometry and the corresponding object trajectory. The components of the scanner assembly that we used for our experiments were also listed.

We determined image quality parameters such as the MTF and NPS of the novel CT system. The results were compared with corresponding parameters that were derived from scans based on the conventional 3rd generation geometry. The same scanner assembly was used for all the scans but the trajectory of X-ray tube, object and detector were modified. An identical sampling density and radiation exposure were applied for the different scanning geometries.

Our approach has shown that the theoretical predictions for the novel CT systems such as contrast enhancement at outer image regions can eventually be kept. This is a consequence of an optimized acquisition of tomographic data without any data processing. Differentiations and classifications of tissues outside the center can be done with a higher statistical confidence, therefore. Moreover, any quantifications such as the determina-

Downloaded From: http://proceedings.spiedigitallibrary.org/ on 08/02/2016 Terms of Use: http://spiedigitallibrary.org/ss/TermsOfUse.aspx

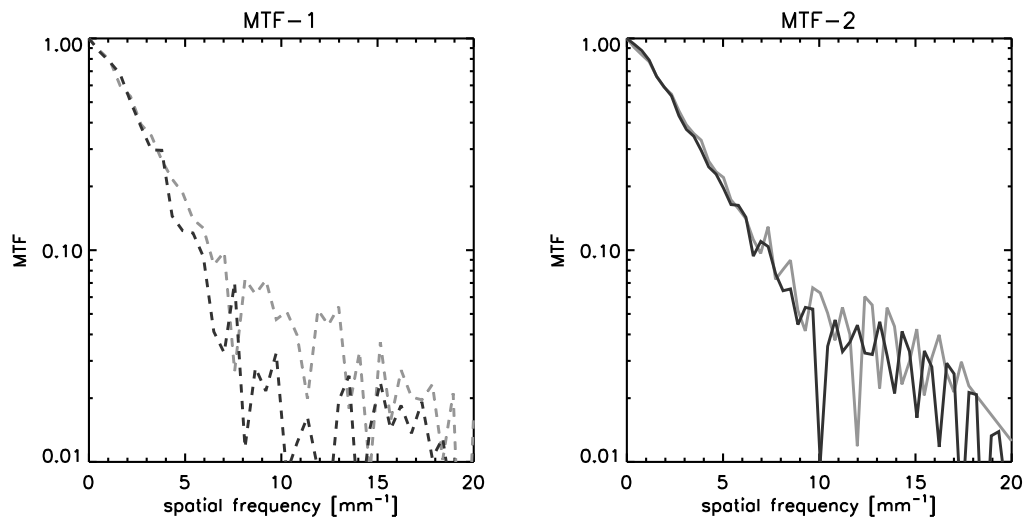

Figure 4. The MTFs that result from different geometries (*light gray line:* watch geometry, *dark gray:* 3rd generation geometry) and from different image positions of the edges used for the determination of the ESFs. The titles of the panels, grayscales, and linestyles correspond to the numbers, scales, and styles used in Fig. 3.

tion of the density of the tissues should become more accurate. We conclude that the combination of the novel geometry with the OPED algorithm provides a higher radiation dose efficiency.

As the distance between object and X-ray source can be modified, the resolving power of the novel CT scanner is changed. The resolving power, i.e., the MTF is determined by the distance of the center C_2 of the object table from the source. Protocols can be performed that start with an overview scan of a larger ROI of the investigated object. Many different scans of smaller ROIs can follow. This is important for the differentiation of smaller papules of tumorous tissues, for instance.

Using our demonstrator and a simulation tool that is based on the Monte-Carlo approach,[11] we aim to develop

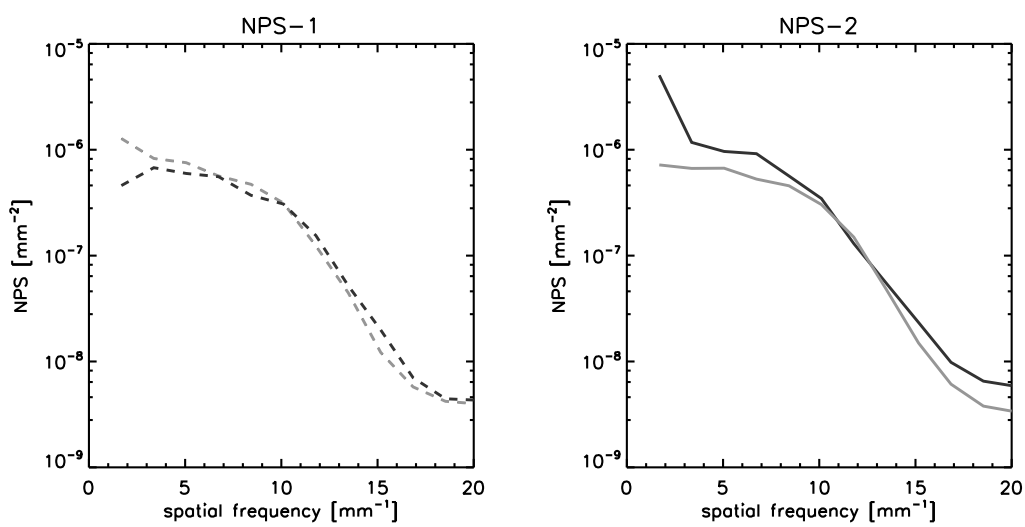

Figure 5. This figure shows the NPS derived from scans of the watch geometry (*light gray line*) and the conventional 3rd generation geometry (*dark gray line*). Solid and dashed lines correspond to the image positions where the NPS are determined. The grayscales and linestyles correspond to the grayscales and styles used in Fig. 3.

Downloaded From: http://proceedings.spiedigitallibrary.org/ on 08/02/2016 Terms of Use: http://spiedigitallibrary.org/ss/TermsOfUse.aspx

methods to correct noise in images derived from the novel CT scanner. Another future objective is to replace the detector system by a more powerful device to produce less noisy images. Furthermore, future investigations that are based on more complex clinical studies where more realistic, anthropomorphic phantoms are used, should be used to test other figures of merits of the novel CT system.

ACKNOWLEDGMENTS

This study about the characterization of the novel CT systems was funded by the Bundesminesterium für Bildung und Forschung (BMBF, German Federal Ministry of Education and Research) through the grant 03NUK008A ("Verbund Kompetenzerhalt Strahlenforschung KVSF: Innovative Verfahren der biomedizinischen Bildgebung zur Optimierung von medizinischen Strahlenanwendungen - Physikalisch-Technische Optimierung und Quantitifizierung von CT-Systemen"). See `www.helmholtz-muenchen.de/kvsf/` for further information.
The development of the demonstrator was funded by grant number 0315189 of the BMBF. We thank H. Schlattl for many fruitfull discussions and acknowledge Philips™ for the delivery of the FBP algorithm they use.

REFERENCES

[1] Deutsches Bundesamt für Umwelt (BMU; German Federal Office for Environment), "Umweltradioaktivität und Strahlenbelastung," 2006.

[2] Deutsches Bundesamt für Strahlenschutz (BfS; German Federal Office for Radiation Protection), "Umweltradioaktivität und Strahlenbelastung im Jahr 2007," 2008.

[3] G. Brix, E. A. Nekolla, and J. Griebel, "Strahlenexposition von Patienten durch diagnostische und interventionelle R" 2005.

[4] A. Stamm-Meyer, D. Noßke, P. Schnell-Inderst, *et al.*, "Diagnostic nuclear medicine procedures in Germany between 1996 and 2002," *Nuklearmedizin* **45**, pp. 1–9, 2006.

[5] D. J. Brenner and E. J. Hall, "Computed tomography – an increasing source of radiation exposure," *N. Engl. J. Med.* **357**, p. 2277, 2007.

[6] D. F. Regulla and H. Eder, "Patient exposure in medical X-ray imaging in Europe," *Radiat. Prot. Dosim.* **114**, pp. 11–25, 2005.

[7] Y. Xu, O. Tischenko, and C. Hoeschen, "A new reconstruction algorithm for radon data," in *Medical Imaging: Image Processing*, M. J. Flynn and J. Hsieh, eds., *Proc. SPIE* **6142**, p. 2A, 2006.

[8] Y. Xu, O. Tischenko, and C. Hoeschen, "Fast implementation of the image reconstruction algorithm OPED," in *Medical Imaging: Image Processing*, M. J. Flynn and J. Hsieh, eds., *Proc. SPIE* **7258**, p. 5F, 2009.

[9] H. de las Heras, O. Tischenko, W. Panzer, Y. Xu, and C. Hoeschen, "Modelling and testing of a non-standard scanning device with dose reduction potential," in *Medical Imaging: Image Processing*, M. J. Flynn and J. Hsieh, eds., *Proc. SPIE* **6510**, p. 3R, 2007.

[10] H. de las Heras, O. Tischenko, B. Renger, Y. Xu, and C. Hoeschen, "Experimental proof of an idea for a CT-scanner with dose reduction potential," in *Medical Imaging: Image Processing*, M. J. Flynn and J. Hsieh, eds., *Proc. SPIE* **6913**, p. O7, 2008.

[11] M. Klaften, A. Schegerer, O. Tischenko, M. Hrabe de Angelis, and C. Hoeschen, "A new design for micro-CT scanner," in *Medical Imaging: Image Processing*, M. J. Flynn and J. Hsieh, eds., *Proc. SPIE* **7258**, p. 5D, 2009.

[12] O. Tischenko, Y. Xu, and C. Hoeschen, "A new scanning device in CT with dose reduction potential," in *Medical Imaging: Image Processing*, M. J. Flynn and J. Hsieh, eds., *Proc. SPIE* **6142**, p. 2L, 2006.

[13] H. Schlattl and C. Hoeschen, "The built-in capacity of CT D'OR's static ring for scatter correction," in *Medical Imaging: Image Processing*, M. J. Flynn and J. Hsieh, eds., *Proc. SPIE* **6913**, p. 52, 2008.

[14] S. W. Rowland, *Computer Implementation of Image Reconstruction Formulas*, 1979.

[15] A. C. Kak and M. Slaney, *Principles of Computerized Tomographic Imaging*, IEEE Press, New York, 1988.

[16] O. Tischenko, M. Klaften, C. Hoeschen, and M. H. de Angelis, "Scanner device and method for computed tomography imaging," 2009. Patent Pub.No. WO/2009/146937.

[17] E. O. Brigham, *The Fast Fourier Transform*, Prentice-Hall Inc., Englewood Cliffs, NJ, 1974.

Downloaded From: http://proceedings.spiedigitallibrary.org/ on 08/02/2016 Terms of Use: http://spiedigitallibrary.org/ss/TermsOfUse.aspx

[18] R. A. Brooks and G. Di Chiro, "Beam hardening in X-ray reconstructive tomography," *Phys. Med. Biol.* **21**, pp. 390–398, 1976.

[19] J. M. Boone, "Determination of the presampled MTF in computed tomography," *Med. Phys.* **28**, p. 356, 2001.

[20] C. Hoeschen, E. Buhr, and W. Döhring, "Determination of the spatial frequency limit of anatomical structures in the x-ray pattern of a thorax examination," *Rad. Prot. Dosim.* **90**, p. 109, 2000.

[21] J. G. Verly and R. N. Bracewell, "Blurring in tomograms made with x-ray beams of finite width," *JCAT* **3**, pp. 662–678, 1979.

[22] S. Doré and Y. Goussard, "Experimental determination of CT point spread function anisotropy and shift-variance," in *IEEE Proceedings*, p. 788, 1997.

[23] C. C. Brunner, S. A. Hurowitz, S. F. Abboud, C. Hoeschen, and I. S. Kyprianou, "Noise characterization of computed tomography using the covariance matrix," in *Medical Imaging: Image Processing*, M. J. Flynn and J. Hsieh, eds., *Proc. SPIE* **subm.**, 2010.

[24] C. J. Bischof and J. C. Ehrhardt, "Modulation transfer function of the EMI CT head scanner," *Med. Phys.* **4**, pp. 163–167, 1977.

[25] P. F. Judy, "The line spread function and modulation transfer function of a computed tomographic scanner," *Med. Phys.* **3**, pp. 233–236, 1976.

[26] H. Fujita, D.-Y. Tsai, T. Itoh, *et al.*, "A simple method for determining the modulation transfer function in digital radiography," *IEEE* **11**, p. 34, 1992.

[27] E. Buhr, S. Günther-Kohfahl, and U. Neitzel, "Accuracy of a simple method for deriving the presampled modulation transfer function of a digital radiographic system from an edge image," *Med. Phys.* **30**, p. 2323, 2003.

[28] I. A. Cunningham and A. Fenster, "A method for modulation transfer function determination from edge profiles with correction for finite-element differentiation," *Med. Phys.* **14**, pp. 533–537, 1987.

[29] International Electrotechnical Commission, "Medical electrical equipment - Characteristics of digital x-ray imaging devices - part1: Determination of the detective quantum efficiency," 2003. IEC 62220-1.

[30] J. T. Dobbins III, D. L. Ergun, L. Rutz, *et al.*, "DQE(f) of four generations of computed radiography acquisition devices," *Med. Phys.* **22**, p. 1581, 1995.

[31] M. F. Kijewski and P. F. Judy, "The noise power spectrum of CT images," *Phys. Med. Biol.* **32**, p. 565, 1987.

[32] H. Illers, *Development of a Standardised Technique for the Measurement of the Detective Quantum Efficiency of Digital X-ray Imaging Systems.* PhD thesis, Technische Universität Carolo-Wilhelmina, Braunschweig, Germany, 2003.

[33] A. L. Kwan, J. M. Boone, K. Yang, and S.-Y. Huang, "Evaluation of the spatial resolution characteristics of a cone-beam breast ct scanner," *Med. Phys.* **34**, p. 275, 2007.

Downloaded From: http://proceedings.spiedigitallibrary.org/ on 08/02/2016 Terms of Use: http://spiedigitallibrary.org/ss/TermsOfUse.aspx